Materials Horizons

ROYAL SOCIETY OF CHEMISTRY

COMMUNICATION

View Article Online
View Journal

Cite this: DOI: 10.1039/d6mh00462h

Received 11th March 2026,
Accepted 29th April 2026

DOI: 10.1039/d6mh00462h

rsc.li/materials-horizons

Nitrogen vacancies in graphitic carbon nitride and their role in heterogeneous photocatalysis

Alessandro Landi, *[a] Francesco Ambrosio, *[b] Nadia Bianchi,[a] Michele Loriso,[b] Lorenzo Malavasi,[c] Antonella Profumo,[d] Julia Wiktor[e] and Andrea Peluso *[a]

Graphitic carbon nitride (g-C_3N_4) is a promising metal-free photocatalyst whose activity is often enhanced by nitrogen vacancies, though their microscopic role remains unclear. Using advanced *ab initio* calculations with large periodic supercells, we show that long-range buckling is essential to correctly evaluate defect energetics and thus determine the stability of distinct vacancy configurations. The most stable defects are found to introduce localized in-gap states corresponding to shallow acceptor and deep donor levels. These features explain (i) the experimental red-shifted absorption and (ii) suppressed photoluminescence observed in N-deficient g-C_3N_4 samples. Most importantly (iii) energy-level alignment at the water–semiconductor interface explains the enhanced photocatalytic reduction and reduced oxidation activity reported experimentally. Overall, our results provide a unified microscopic picture that quantitatively connects defect-induced electronic structure changes and experimental observables, offering a concrete predictive strategy for designing defect engineered carbon nitride and related metal-free photocatalysts.

New concepts

Defect engineering has emerged as a cornerstone strategy for tuning the photocatalytic performance of graphitic carbon nitride (g-C_3N_4), yet the field has long lacked a unified microscopic picture connecting atomic-scale vacancy structures to measurable device-level outcomes. The prevailing approach – modelling defects in small, idealized flat supercells – misses a physically crucial ingredient: the long-range, collective out-of-plane buckling that is intrinsic to this two-dimensional material. This work introduces the concept that structural corrugation is not a minor geometric detail but a thermodynamic factor that dictates which nitrogen vacancies actually form and dominate in real samples. By using hybrid density functional theory on supercells exceeding one thousand atoms, we demonstrate that neglecting long-range buckling can even invert the predicted stability ordering of competing defect configurations – a qualitative error with direct consequences for interpreting experiments. Beyond structural insights, the framework establishes, for the first time, a quantitative and self-consistent link between defect-induced electronic levels and three distinct classes of experimental observables: red-shifted optical absorption, photoluminescence quenching, and the asymmetric enhancement of photo-reduction *versus* suppression of photo-oxidation activity. This "defect-to-function" predictive protocol is transferable to other two-dimensional carbon nitrides and metal-free photocatalysts, offering the materials community a rigorous computational protocol for rationally engineering defective semiconductors with precisely tailored optoelectronic and catalytic selectivity.

Introduction

Graphitic carbon nitride (g-C_3N_4) is a metal-free semiconductor with remarkable potential for sustainable technologies.[1–3] It is composed of fused heptazine (tri-*s*-triazine) units (see Fig. 1) and can be synthesized inexpensively *via* thermal condensation of nitrogen-rich precursors (*e.g.* melamine or urea).[4,5] This facile, low-cost preparation yields a chemically and thermally stable layered network that exhibits a moderate band gap ($\approx$2.7–2.8 eV) enabling visible-light absorption. These properties, together with a tunable electronic structure, make g-C_3N_4 attractive for a wide range of applications,[3] such as energy storage devices,[4] organic electronics,[6,7] and sensors.[8,9]

In particular, g-C_3N_4 has been extensively studied[5] for photocatalytic applications including solar-driven hydrogen evolution,[10,11] CO_2 reduction,[12] and organic pollutant degradation.[13–19] In this framework, very recently, g-C_3N_4 has also been investigated for its potential use in photocatalytic nitrogen fixation, *i.e.*, reduction of gaseous N_2 to ammonia (NH_3) operated by sunlight, one among the most arduous and rewarding tasks in the field of heterogeneous photocatalysis.[20,21]

[a] *Dipartimento di Chimica e Biologia Adolfo Zambelli, Università di Salerno, Via Giovanni Paolo II, I-84084, Fisciano, SA, Italy. E-mail: alelandi1@unisa.it*
[b] *Dipartimento di Scienze, Università degli Studi della Basilicata, Viale dell'Ateneo Lucano, 10, 85100, Potenza, Italy. E-mail: francesco.ambrosio@unibas.it*
[c] *Energy and Materials Chemistry Group, Department of Chemistry and INSTM, University of Pavia, Via Taramelli 16, Pavia, 27100, Italy*
[d] *Department of Chemistry, University of Pavia, Via Taramelli 16, Pavia, 27100, Italy*
[e] *Department of Physics, Chalmers University of Technology, SE-412 96, Gothenburg, Sweden*

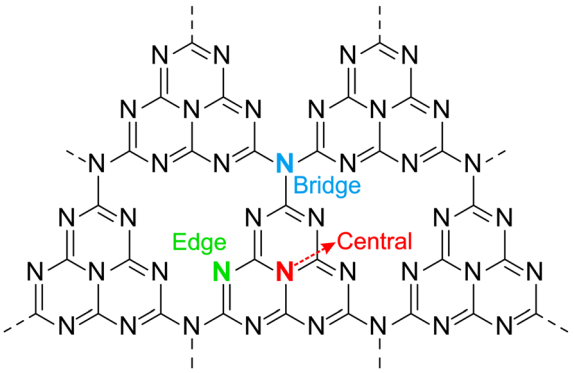

Fig. 1 Pictorial representation of the *P6/m2* heptazine-based network, highlighting, by color code, the nitrogen sites where vacancies can occur.

Although nitrogen fixation is challenging due to the high stability of the N–N triple bond, the layered structure of g-C_3N_4 and its nitrogen-rich framework make it amenable to defect engineering and heterojunction formation, which, in turn, enable its employment as a photocatalyst for promoting N_2 activation. Nevertheless, its photocatalytic performance is limited by poor intrinsic conductivity, rapid charge–carrier recombination, and a low density of active sites for N_2 adsorption and reduction.[22,23] In this context, strategies such as intrinsic defect engineering, heteroatom doping, and heterojunction formation have proved to be effective in the modulation of the electronic structure by introducing in-gap states that extend visible-light absorption, enhance charge separation, and ultimately improve photocatalytic efficiency.[2,3,13–19,24–28]

Among intrinsic defects, nitrogen vacancies (V_N) have received particular attention: various methods have been developed to control their concentration in the sample, either using precursors yielding vacancy-rich structures[29,30] or *via* post-synthesis thermal treatments.[31] From a microscopic perspective, nitrogen vacancies are not all chemically equivalent, as they can be formed in three distinct locations of the heptazine-based network, corresponding to the removal of a neutral nitrogen atom (i) at the center of heptazine, V_N^0(C), (ii) on the edge of the fused rings, V_N^0(E), and (iii) bridging two units in the periodic 2D lattice V_N^0(B), see Fig. 1. These should be considered as different defects, possibly giving distinct chemical behavior and electronic signatures.[31–33]

Since the nature of the probed defects at the atomistic level is beyond reach for experimental characterization, theoretical and computational efforts have been deployed to unveil the defect physics underlying the measured properties.[2,16,31,34,35] However, current studies do not provide a microscopic physical picture always fully consistent with the experimental characterization. This could be related to several factors, such as employing relatively small supercells for the simulations, as has been done in several works,[31,35] often assuming an idealized, perfectly flat layer. However, in two-dimensional materials, corrugation is known to significantly affect the structural and electronic properties[36–38]; such an effect may be extended over large distances, thus requiring sufficiently large supercells to be properly accounted for.[39] In particular, buckling in g-C_3N_4 is known to relieve electrostatic repulsion between lone pairs on adjacent nitrogen atoms, thereby stabilizing the structure.[40] Thus, a correct description of corrugation in g-C_3N_4 is essential for an accurate prediction of adiabatic and vertical charge-transition levels, together with defect reorganization energies, all features required to provide a reliable microscopic interpretation of the vast body of spectroscopic and photocatalytic studies conducted on N-deficient g-C_3N_4.[3,31,32,41–49]

Motivated by these challenges, we investigate herein the electronic structure of g-C_3N_4 containing N vacancies, using periodic supercell calculations based on advanced hybrid density functional theory (DFT). Our approach fully accounts for the effects of corrugation and its size-dependence, to achieve both convergence of electronic properties and a robust description of the defect energetics, enabling identification of the most stable moieties. This framework allows us to connect the calculated properties with a plethora of experimental observations: first and most important, (i) we rationalize the activity of N-deficient g-C_3N_4 towards photo-reduction and photo-oxidation in terms of the alignment between defect energy levels and relevant redox potentials. Moreover, we attribute either (ii) experimental red-shifted absorption and (iii) the measured photoluminescence quenching in N-deficient samples to deep in-gap donor levels, arising from charge localization at the vacancy site.

To this end, we employ hybrid DFT including non-local electron correlation effects (see section S1, SI) – a computational approach previously applied to a broad range of π-conjugated systems (including fullerenes, covalently bonded fullerene networks,[50] and acenes[51,52]) – to investigate pristine and N-deficient monolayer g-C_3N_4.

As an initial model for the pristine material, we adopt the idealized flat *P6/m2* heptazine-based network (Fig. S1, SI) proposed by Teter and Hemley,[53] which is widely used as a repeating unit for the fully condensed system.[54] Supercells of the 2D monolayer with increasing size are then constructed by replicating n times (where n = 2, 4, and 6) the unit cell along the a and b directions. In the following, these supercells are denoted as 2 × 2, 4 × 4, and 6 × 6, respectively. The latter comprises up to 1008 atoms (see Table S1 for details), a system size at the forefront of the current state of the art.

Structural relaxation of initially planar g-C_3N_4 monolayers invariably leads to buckled configurations, irrespective of supercell size, accompanied by a substantial lowering of the total energy relative to the planar geometry (Table S2, SI). Although the Mermin–Wagner theorem predicts the instability of long-range planar order at finite temperature,[55,56] the emergence of buckling already at the DFT level (0 K) can be rationalized by partial relief of angular strain in N-containing bonds and a reduction of lone-pair repulsion.[38,57,58] Analysis of the relaxed structures reveals a pronounced supercell-size dependence of the out-of-plane distortions. The 2 × 2 supercell exhibits only modest corrugation, with a mean absolute height (MAH $= \frac{1}{N}\sum_i |h_i|$, h_i being the signed distance of each atom i

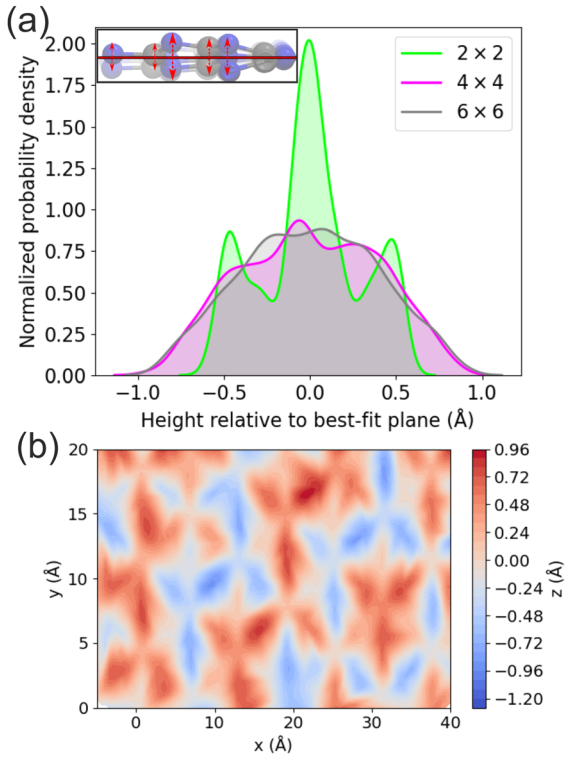

Fig. 2 (a) Comparison of the distribution of out-of-plane atomic distortions with respect to the mean plane (see the inset) for the three supercells under study. (b) Contour plot visualizing the atomic z-coordinate variations across the (x, y) plane in the 4 × 4 relaxed g-C_3N_4 structure. See also Fig. S4 in the SI.

from the plane, see the SI) of 0.23 Å, a largest buckling amplitude (LBA = $\max_i(h_i) - \min_i(h_i)$) of 1.08 Å (see the SI for details), and a narrow distribution of atomic displacements (Fig. 2a). In contrast, the 4 × 4 and 6 × 6 supercells display significantly larger and broadly distributed distortions, with MAH = 0.33 Å and LBA = 1.79 Å (Fig. 2a). Contour plots of the atomic z coordinates across the (x, y) plane further reveal a periodic buckling pattern, indicative of a delocalized and ordered corrugation rather than isolated protrusions (Fig. 2b). In the SI (Fig. S4), we report the same contour plot with the projected atomic positions overlayed to clarify which atoms are associated with out-of-plane distortions. Comparison of different supercells (Fig. S3 and S4) shows that the 2 × 2 cell cannot fully accommodate the long-range nature of the buckling, as evidenced by its altered corrugation periodicity, while the 4 × 4 supercell emerges as the minimal size required to achieve reasonably converged structural properties.

Next, we move on to the characterization of the neutral N vacancy, V_N^0, considering its possible different positions, see Fig. 1. To evaluate how buckling affects the defect energy, we consider the removal of one N from 2 × 2, 4 × 4, and 6 × 6 supercells. Then, for each defect in each supercell, we perform structural relaxations in three different ways: either (i) enforcing the initial planarity of the 2D system by constraining the position of the nuclei on the z axis; (ii) fully relaxing the supercell, leading to buckled structures (much more stable than planar configurations, Table S2, SI); and (iii) building 4 × 4 and 6 × 6 models as replicas of the corrugated pristine 2 × 2 supercell.

In this latter case, the 2 × 2 buckling is preserved by fixing the z coordinate during relaxation after removing one nitrogen atom to create the vacancy. This system is used to separate the effects on the total energy arising from different corrugations in different supercells, from that of local defect relaxation, and from possible electrostatic finite-size effects due to excitonic charge localization at the defect.[59]

For each model, we compare the relative stability of V_N^0(C), V_N^0(E), and V_N^0(B). The results are collected in Table 1 and refer to the doublet spin state of V_N^0, which is always found to be lower in energy by more than 1.5 eV, with respect to the quartet state (Table S3, SI).

Inspection of Table 1 immediately reveals that V_N^0(B) is consistently the least stable defect. This instability arises from the substantial structural reorganization induced by this vacancy, which involves significant distortion of the dangling heptazine units; notably, one unit tilts almost perpendicularly to the plane of the material layer, see Fig. 3. Such a pronounced relaxation comes at a high elastic cost, thus explaining the poor stability of this defect with respect to the other ones for all the considered systems, particularly when planarity is forced. Therefore, in the following discussion, we focus mainly on the competition between V_N^0(C) and V_N^0(E).

Our results indicate that the relative stability of these latter two defects is highly dependent on the local structure around the N vacancy. This, in turn, is connected with the degree of buckling allowed by the supercell size. First, the results obtained for the constrained planar structures show that the edge defect is by far the most stable, with energy differences up to 1 eV with respect to the central vacancy, see Table 1. Conversely, when considering the buckled structures, V_N^0(C) is found to be the most stable N vacancy in the 2 × 2 supercell, see Table 1. However, we observe a remarkable inversion in relative stability when moving to the 4 × 4 supercell: the total energy of V_N^0(E) is found to be 0.57 eV lower than that of V_N^0(C). This trend appears to be fairly converged for the 6 × 6 supercell. Finally, V_N^0(C) and V_N^0(E) become almost iso-energetic in both 4 × 4 and 6 × 6 supercells, when keeping the corrugation fixed to that of the pristine 2 × 2 cell, thus highlighting the importance of local structural relaxations in conjunction with global corrugation of the material. Taken together, the results achieved for different models clearly indicate that (i) out-of-plan distortions, both

Table 1 Relative energy (in eV) for V_N^0 in central (C), edge (E) and bridge (B) position, as calculated for different supercell sizes of g-C_3N_4 monolayer models and considering ideal planar, fully relaxed (buckled) and replicas of 2 × 2 buckling structural configurations (*vide infra*)

Structure	Planar			Buckled			2 × 2 replicas		
V_N^0	C	E	B	C	E	B	C	E	B
2 × 2	+0.79	0.00	+3.49	0.00	+0.54	+1.49	0.00	+0.03	+2.48
4 × 4	+0.80	0.00	+3.24	+0.57	0.00	+1.12	+0.02	0.00	+1.88
6 × 6	+1.01	0.00	+3.30	+0.60	0.00	+1.20	+0.01	0.00	+1.81

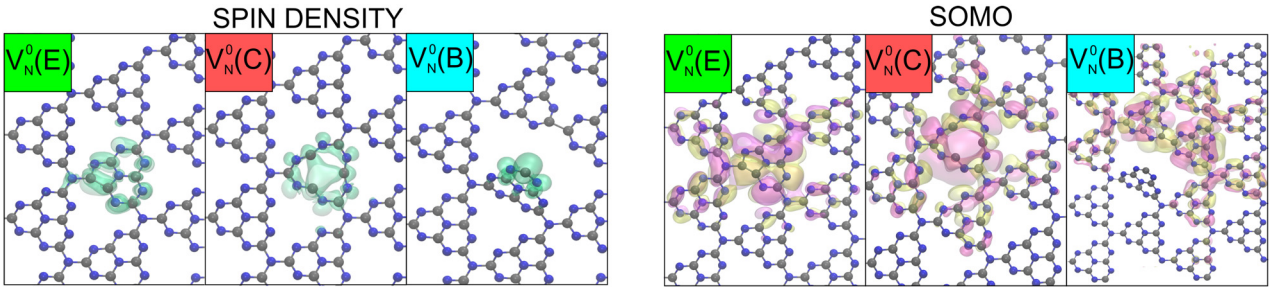

Fig. 3 Stick and ball top-view representation of the 4 × 4 g-C_3N_4 monolayer bearing a neutral N vacancy in different positions: central (left panel), edge (middle panel) and bridge (right panel). C and N atoms are colored in grey and blue, respectively. The isodensity representations of the spin density are shown in green (isovalue 0.001 a.u.) in the three left panels, while isodensity representations of the singly occupied molecular orbitals (SOMO) are illustrated in magenta and yellow in the three panels on the right.

locally induced by the defect and naturally ensuing from pristine g-C_3N_4, determine the relative stability of different defects and (ii) the reduced corrugation available for small supercells may lead to an incorrect evaluation of the defect's relative stability.

By inspecting the local structure of the different defects in the buckled supercells, we observe that the removal of the central N atom in V_N^0(C) results in the formation of a 5-membered ring fused with a larger 9-membered ring for the 2 × 2 cell (Fig. S6, SI), while an extended ring involving the whole heptazine unit is found for both 4 × 4 (Fig. 3) and 6 × 6 systems, thus further proving how a small supercell may provide incorrect local structures. In contrast, V_N^0(E), for any supercell size, is always found to feature reorganization of the local bonding into a small 5-membered ring upon formation of a bond between the dangling C atoms, adjacent to the vacancy, see Fig. 3. This ring, comprising two carbon and two nitrogen atoms together with the C–C bond formed at the defect site, is topologically analogous to an imidazole-type heterocycle, and its formation reflects the tendency of the unsaturated carbon centers to recover a locally aromatic coordination environment.

The introduction of nitrogen vacancies leads to a reduction in the degree of buckling of the g-C_3N_4 layer. In particular, for the central defect, the two-dimensional height map (Fig. S5) reveals that the characteristic periodic distortions observed in the pristine structure are largely suppressed near the defect site, giving rise to a more planar morphology. This flattening effect suggests that the removal of a nitrogen atom locally relieves internal strain, leading to an extended ring structure that is more stabilized in the absence of long-range out-of-plane distortions. Conversely, for the external defect, V_N^0(E), this effect is lower as the replacement of one 6-atom ring with a 5-atom ring has a reduced impact on the global structure of g-C_3N_4. Therefore, V_N^0(E), with its more compact structure, better fits inside the natural distortions of the two-dimensional network, see Fig. S5, thus justifying its greater stability.

We next focus on the electronic properties, calculated for the 4 × 4 supercell, which showed a fairly converged structure and energetics. First, from inspection of the spin density as well as from the frontier orbitals (Fig. 3 and Fig. S6 and S7), we observe that (i) all the three types of vacancies show spin localization on the defective heptazine unit; (ii) V_N^0(C) and V_N^0(E) also present a localized Kohn–Sham energy level in the band gap of the material (see also Fig. S2 in the SI). Therefore, from an electronic-structure perspective, all three defects could, in principle, be related to the observed EPR spectra.[60] However, only V_N^0(C) and V_N^0(E) may provide charge localization, which can be responsible for boosting the photocatalytic activity of g-C_3N_4 samples.[61] Therefore, in the following, we focus on the electronic structure and the energy levels associated only with V_N^0(E) and V_N^0(C). It is important to mention that although the calculated energetics would suggest dismissing the central vacancy as a relevant defect in isolated g-C_3N_4, the extent of buckling may depend on interactions between g-C_3N_4 and an underlying substrate when forming a heterojunction. Such interfacial interactions in experimentally realized heterostructures or chemically modified samples could, in principle, alter the corrugation pattern and thereby modify the relative defect stability.

Starting from the neutral defects, we next determine whether they can accept and/or donate electrons. To this end, we consider both positively and negatively charged vacancies, V_N^+ and V_N^-, respectively, for central and edge defects. For V_N(C), we observe a sizable reconstruction of the 9-membered ring, upon oxidation/reduction, see Fig. 4. In particular, injection of an electron leads to tightening of the honeycomb-like structure, closer to that of the original pristine heptazine unit. At variance with this, electron detachment is found to further enhance the reconstruction of the 9-atom ring, observed for the neutral defect, leading to a swollen and rounder moiety. For V_N(E), on the other hand, the reorganization of the edge defect upon variation of charge states is much more localized, involving mainly the C–C bond observed for the neutral system (Fig. 4). This bond is found to shorten from 1.61 to 1.49 Å upon reduction, while it breaks in the oxidized defect.

Spin-polarized calculations show that singlet configurations are strongly favored over triplets, by ≈1 eV in the +1 state and ≈0.6 eV in the −1 state, see Table S3. These large singlet–triplet splittings preclude thermal population of triplet states. These results are still compatible with the experimental reports of triplet involvement inferred under photo-excitation, which must originate from non-equilibrium excited-state processes.[62] It is also worth noting that, while the relative stability of V_N(C) and

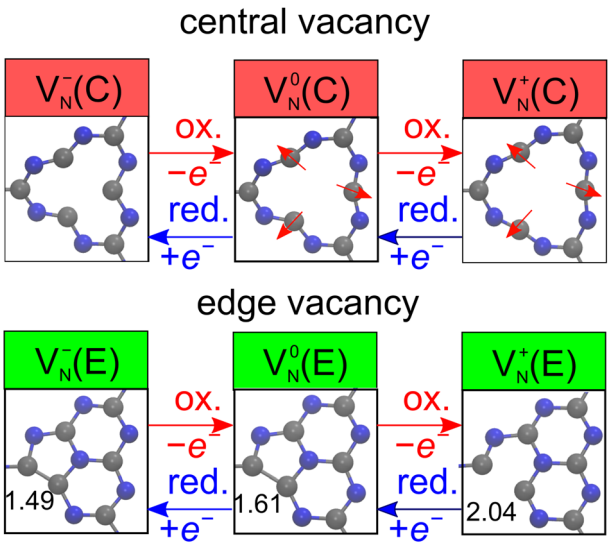

Fig. 4 Stick and ball representation of the local structure for central and edge N vacancies in monolayer g-C_3N_4 at varying charge states. Red arrows in the top panels indicate the breathing motion of the 12-atom ring of the central defect, while in the bottom panels we report the variation of the relevant C–C distance (in Å) for the edge defect.

V_N(E) defects estimated for the neutral vacancy is preserved for the reduced species, an opposite trend is observed for the oxidized defect, for which the V_N(C) structure is found to be favored by as much as 0.35 eV (Table S4). However, under typical synthesis conditions, g-C_3N_4 is intrinsically n-type, favoring neutral or negatively charged nitrogen vacancies.[63] The positively charged central vacancy would become thermodynamically favorable only under strongly p-type conditions, which are not commonly realized in as-grown materials.[28] The possibility of V_N^+(E) → V_N^+(C) interconversion upon photoexcitation should also be ruled out, as a sizable barrier is expected for the migration of a tri-coordinated N atom. This implies that, once formed, each defect configuration is indeed kinetically frozen.

We now turn to the calculation of the charge transition levels (CTLs) associated with the investigated nitrogen vacancies, employing the grand-canonical formalism for defects in crystalline semiconductors[64–66] (see Section S2 of the SI). The resulting values, reported in Table 2 and Fig. 5 and 6, define the thermodynamic stability of the different charge states and provide the basis for interpreting the photocatalytic and spectroscopic behavior of defective g-C_3N_4.

Impact on photocatalysis

The V_N^0(C) and V_N^0(E) defects feature (0/−) CTL at 2.63 and 2.59 eV above the valence band maximum (VBM), respectively. Considering the calculated and experimental gap of 2.7 eV,[17] these are shallow acceptor levels at ≈0.1 eV below the conduction band minimum (CBM) of g-C_3N_4 (see Fig. 6). Such levels are consistent with the improved visible absorption and moderate carrier trapping observed for g-C_3N_4 samples with mild concentrations of N vacancies.[31,32] At variance, the adiabatic (+/0) levels are found at 1.70 and 0.82 eV above the VBM of

Table 2 Calculated adiabatic (μ^{ad}) and optical vertical $\left(\mu^{opt}_{q\to q'}\right)$ CTL for central and edge V_N defects, along with corresponding reorganization energies, $\lambda_{q\to q'}$. q and q' denote the initial and final charge states. Adiabatic CTLs refer to fully relaxed initial and final geometries, whereas vertical CTLs are evaluated at fixed geometries (see the SI). All values are given in eV relative to the VBM (set to 0 eV)

Defect	μ^{ad}		$\mu^{opt}_{q\to q'}$				$\lambda_{q\to q'}$			
Position	(0/−)	(+/0)	0 → −	− → 0	0 → +	+ → 0	0 → −	− → 0	0 → +	+ → 0
Central	2.63	1.70	3.33	2.20	0.65	2.32	0.70	0.43	1.05	0.62
Edge	2.59	0.82	2.80	1.87	0.29	1.51	0.21	0.62	0.53	0.69

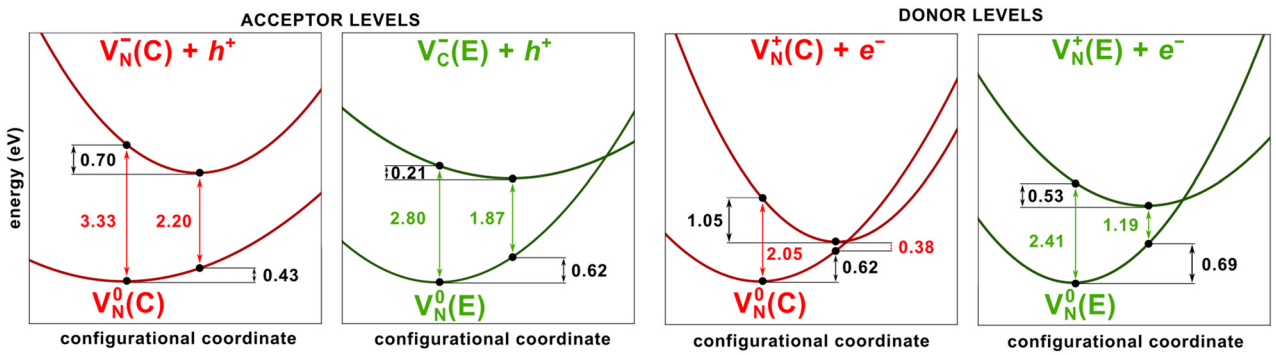

Fig. 5 Calculated configuration coordinate diagrams for central and edge N vacancies in g-C_3N_4. The two left panels refer to recombination of a hole with the reduced defect (*via* acceptor levels), while the two right panels to recombination of an electron with the oxidized vacancy (*via* donor levels).

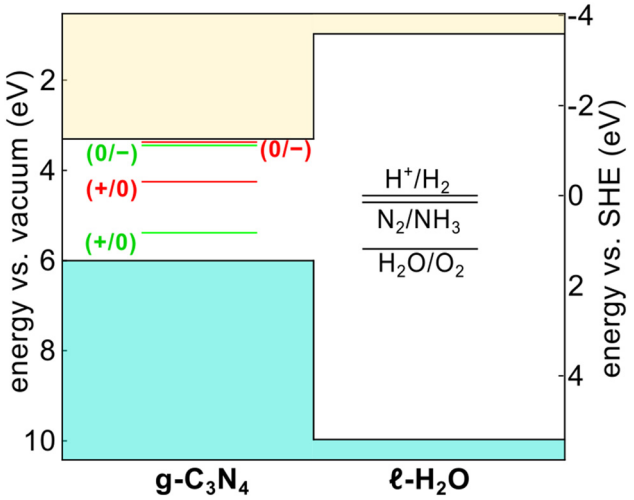

Fig. 6 VBM and CBM of g-C_3N_4 aligned with (i) the band edges of liquid water (ℓ-H_2O) and (ii) the redox levels associated with aqueous proton reduction, nitrogen fixation, and water oxidation. Energies are reported relative both to the vacuum level and the computational standard hydrogen electrode (SHE) of ref. 67 and 68. The VBM and CBM of g-C_3N_4 lie 6.00 and 3.30 eV below the vacuum level, respectively.[17] The corresponding band-edge positions of liquid water (9.97 and 0.97 eV *vs.* vacuum) are taken from ref. 68. Adiabatic charge transition levels of defects (0/+) and (0/−) in the band gap of g-C_3N_4 are aligned to the VBM of g-C_3N_4 as reported in Table 2; red and green lines correspond to V_N(C) and V_N(E) vacancies, respectively.

g-C_3N_4, for V_N(C) and V_N(E), respectively, both representing deep donor defects in the band gap.

To assess the implications for photocatalysis, in Fig. 6 we also report the alignment of these adiabatic defect levels at the semiconductor–water interface, taking advantage of the band alignment from ref. 17. The redox potential of reactions typically targeted by photocatalysis, *i.e.* H_2 production, N_2 fixation, and water oxidation, is included for comparison. That alignment evidences that acceptor levels for both central and edge defects are favorably positioned against H^+/H_2 and N_2/NH_3 potentials. This, coupled with the shallow trapping of electrons, is expected to promote electron transfer toward reduction reactions, thereby enhancing photo-reduction yields.

Conversely, holes trapped at the vacancy site are associated with deep donor levels that lie far above the H_2O/O_2 oxidation potential, deteriorating the otherwise favorable alignment between the pristine VBM and the water oxidation level. The overall picture is in full agreement with the available experimental evidence that N-deficient g-C_3N_4 increases the yield of photo-reduction reactions but worsens performances towards photo-oxidation processes.[42–49]

Interpretation of UV absorption spectra

We now analyze the vertical energy levels to rationalize defect-mediated UV-vis transitions. As shown in the configurational coordinate diagrams (Fig. 5) two excitation channels can be considered: (i) for acceptor-like defects, we consider excitation of an electron from the valence band of g-C_3N_4 to the defect level, VBM → (0/−) CTL. Conversely, for donor-like defects, we consider excitation from the defect level to the conduction band: (0/+) → CBM.

The VBM → (0/−) vertical transition fall at ΔE values of 3.3 eV and 2.8 eV for the central and edge defects, respectively, very close to the experimental gap of pristine g-C_3N_4 (2.7–2.9 eV[4,5]). Thus, this transition does not introduce a significantly lower-energy absorption channel and cannot account for the experimentally observed reduction of the optical gap (2.0–2.5 eV)[31,32,41] in defective samples. In contrast, vertical excitation of an electron from the oxidized defect (0/+) to the CBM (after inclusion of excitonic effects, which decrease the gap by 0.32 eV, *cf.* the SI) yields a ΔE value of 1.73 eV for the central defect and 2.09 eV for the edge defect; the latter is in excellent agreement with the gap of defective g-C_3N_4.

In other words, among the four charge-transition levels considered, only the (+/0) → CBM transition associated with the edge vacancy remains consistent with the experimentally observed absorption range for defective samples e g-C_3N_4; therefore, we conclude that (i) the spectroscopic signatures of N vacancies in g-C_3N_4 originate from donor-type transitions, and (ii) these experimental absorption features can be attributed to the edge vacancy V_N(E), thus corroborating our previous analysis of defect energetics.

Photoluminescence quenching

Finally, both vertical and adiabatic quantities provide insight into the experimentally observed photoluminescence quenching in N-deficient carbon nitride.[31,32,41] First of all, as discussed above, donor levels are located deep into the band gap, possibly enhancing non-radiative recombination channels and thus reducing photoluminescence.[31,32,41]

Furthermore, for all considered defects, the peak energies of the optical transitions differ markedly from the corresponding adiabatic charge transition levels (Table 2 and Fig. 5). This difference originates from the pronounced structural relaxation upon oxidation or reduction (Fig. 4), which results in sizable reorganization energies (Table 2). The effect is particularly pronounced for the (+/0) transition, where $\lambda_{q\to q'}$ reaches 1.05 eV for the central defect, but in general, except for the reduction of the edge defect where λ is comparatively small (0.21 eV), all charge-state changes involve substantial lattice rearrangements. The resulting wide separation of the potential-energy surfaces favors non-radiative multi-phonon relaxation over radiative recombination, providing a natural explanation for the experimentally reported photoluminescence quenching in N-deficient g-C_3N_4.[31,32,41] In this regard, we note that reorganization energies below 0.1 eV are calculated for the relaxation of charge carriers in the pristine material, as a consequence of a larger delocalization of both holes and electrons, *cf.* Fig. S10 and Section S8 of the SI. Therefore, we predict a small difference between the vertical and adiabatic band gap of pristine g-C_3N_4, which is consistent with the red shifts below 0.1–0.2 eV observed in emission spectra and the small separation between potential energy surfaces agrees with the absence of PL quenching in pristine samples.[17]

In conclusion, we carried out a systematic *ab initio* study establishing a comprehensive framework for understanding nitrogen vacancies in g-C_3N_4. By performing advanced DFT calculations on systems exceeding a thousand atoms, we showed that convergence of long-range buckling is essential for correctly predicting both the relative stability and electronic properties of defects, as small supercells fail to capture the collective out-of-plane distortions that stabilize pristine and defective systems, an effect often overlooked in prior studies. Calculated adiabatic and optical charge transition levels enable direct comparison with experiments, reproducing the red-shifted absorption (2.0–2.5 eV) and connecting large reorganization energies (up to 1.05 eV) with photoluminescence quenching and shortened emission lifetimes in N-deficient samples. Most importantly, band alignment at the semiconductor–water interface rationalizes the observed enhancement of photo-reduction reactions alongside deteriorated photo-oxidation performance, linking defect energetics to catalytic selectivity. To our knowledge, this is the first theoretical study to comprehensively correlate the calculated defect properties of g-C_3N_4 with multiple important experimental observables, such as absorption spectra, photoluminescence behavior, and photocatalytic efficiency. By connecting an atomic-scale defect structure with macroscopic performance, our work provides a predictive framework protocol for rational design of defect-engineered g-C_3N_4 with tailored optoelectronic and catalytic properties. Furthermore, our computational methodology can be extended both to (i) other defect types (carbon vacancies and dopants) and (ii) related two-dimensional carbon nitride materials, making it a general and transferable tool for predictive modeling and targeted optimization of (metal-free) photocatalysts.

Conflicts of interest

There are no conflicts to declare.

Data availability

The data supporting this article have been included as part of the Supplementary information (SI). Supplementary information contains computational details of the DFT methodology and charge transition levels calculations; validation of the hybrid functional and robustness of defect charge-transition levels; structural, energetic, and statistical analyses of buckling in pristine and defective g-C_3N_4; spin-state energetics, optimized geometries, and SOMO isodensity plots for different supercells containing neutral nitrogen vacancies; details about electrostatic finite-size corrections for charged defects; relative stability and spin configurations of charged central and edge nitrogen vacancies. See DOI: https://doi.org/10.1039/d6mh00462h.

Acknowledgements

A.L. acknowledges PRIN 2022 grant 2022XSC9P5 (INTESA-SOLE) by Ministero of Università e Ricerca (MIUR) and the FARB 2025 grant from Università di Salerno for funding. F.A. and M.L. acknowledge the PRIN 2022-PNRR grant (P2022W9773) for funding. A.L., F.A. and M.L. acknowledge the CINECA award under the ISCRA initiative, for high-performance computing resources: projects MHP-DEF and Photofix. J.W. acknowledges funding from the Swedish Strategic Research Foundation through a Future Research Leader programme (FFL21-0129), the Swedish Research Council (2019-03993), the European Research Council (ERC Starting Grant no. 101162195), and the Knut and Alice Wallenberg Foundation (2023.0032 and 2024.0042). A.P. acknowledges PRIN 2022 grant 2022TWKM4X.

References

1 G. O. Hartley and N. Martsinovich, *Faraday Discuss.*, 2021, **227**, 341–358.
2 M. Chen, M. Sun, X. Cao, H. Wang, L. Xia, W. Jiang, M. Huang, L. He, X. Zhao and Y. Zhou, *Coord. Chem. Rev.*, 2024, **510**, 215849.
3 J. Lin, W. Tian, H. Zhang, H. Sun and S. Wang, *Acc. Chem. Res.*, 2024, **57**, 2303–2315.
4 M. Subbiah, A. Mariappan, A. Sundaramurthy, S. Venkatachalam, R. T. Renganathan, N. Saravanan, S. Pitchaimuthu and N. Srinivasan, *ACS Omega*, 2024, **9**, 11273–11287.
5 N. T. T. Ha, P. T. Be, P. T. Lan, N. T. Mo, L. M. Cam and N. N. Ha, *RSC Adv.*, 2021, **11**, 16351–16358.
6 H. Y. Hoh, Y. Zhang, Y. L. Zhong and Q. Bao, *Adv. Opt. Mater.*, 2021, **9**, 2100146.
7 J. Bian, C. Huang and R. Zhang, *ChemSusChem*, 2016, **9**, 2723–2735.
8 R. Malik, N. Joshi and V. K. Tomer, *Coord. Chem. Rev.*, 2022, **466**, 214611.
9 L. Chen and J. Song, *Adv. Funct. Mater.*, 2017, **27**, 1603605.
10 R.-H. Gao, Q. Ge, N. Jiang, H. Cong, M. Liu and Y.-Q. Zhang, *Front. Chem.*, 2022, **10**, 1048504.
11 S. Yang, Y. Gong, J. Zhang, L. Zhan, L. Ma, Z. Fang, R. Vajtai, X. Wang and P. M. Ajayan, *Adv. Mater.*, 2013, **25**, 2452–2456.
12 S. Bhowmik, S. J. Phukan, N. K. Sah, M. Roy, S. Garai and P. K. Iyer, *ACS Appl. Nano Mater.*, 2021, **4**, 12845–12890.
13 M. Corti, R. Chiara, L. Romani, B. Mannucci, L. Malavasi and P. Quadrelli, *Catal. Sci. Technol.*, 2021, **11**, 2292–2298.
14 M. Medina-Llamas, A. Speltini, A. Profumo, F. Panzarea, A. Milella, F. Fracassi, A. Listorti and L. Malavasi, *Nanomaterials*, 2023, **13**, 263.
15 J. Pei, H. Li, D. Yu and D. Zhang, *Catalysts*, 2024, **14**, 825.
16 C. Tedesco, L. Gregori, A. Simbula, F. Pitzalis, A. Speltini, F. Merlo, S. Colella, A. Listorti, E. Mosconi, A. A. Alothman, W. Kaiser, M. Saba, A. Profumo, F. De Angelis and L. Malavasi, *Adv. Energy Sustainability Res.*, 2024, **5**, 2400040.
17 L. Romani, A. Speltini, C. N. Dibenedetto, A. Listorti, F. Ambrosio, E. Mosconi, A. Simbula, M. Saba, A. Profumo, P. Quadrelli, F. De Angelis and L. Malavasi, *Adv. Funct. Mater.*, 2021, **31**, 2104428.

18 Y. Baghdadi, F. Temerov, J. Cui, M. Daboczi, E. Rattner, M. S. Sena, I. Itskou and S. Eslava, *Chem. Mater.*, 2023, **35**, 8607–8620.
19 Y. Baghdadi, M. Daboczi, F. Temerov, M. Yang, J. Cui and S. Eslava, *J. Mater. Chem. A*, 2024, **12**, 16383–16395.
20 R. Huang, X. Li, W. Gao, X. Zhang, S. Liang and M. Luo, *RSC Adv.*, 2021, **11**, 14844–14861.
21 X.-C. Tang, Z. Ding, Z.-H. Wang, N. Arif, Y.-Y. Chen, L. Li and Y.-J. Zeng, *ChemCatChem*, 2024, **16**, e202401355.
22 L. Zhang, S. Hou, T. Wang, S. Liu, X. Gao, C. Wang and G. Wang, *Small*, 2022, **18**, 2202252.
23 G. Dong, W. Ho and C. Wang, *J. Mater. Chem. A*, 2015, **3**, 23435–23441.
24 Y. Zhang, T. Mori, J. Ye and M. Antonietti, *J. Am. Chem. Soc.*, 2010, **132**, 6294–6295.
25 P. Niu, G. Liu and H.-M. Cheng, *J. Phys. Chem. C*, 2012, **116**, 11013–11018.
26 J. Fu, J. Yu, C. Jiang and B. Cheng, *Adv. Energy Mater.*, 2018, **8**, 1701503.
27 A. Landi, G. Ricci, Y. Olivier, A. Capobianco and A. Peluso, *J. Phys. Chem. Lett.*, 2024, **15**, 11042–11050.
28 Y. Zhang, P. Lian, X. Hao, L. Zhang, L. Yang, L. Jiang, K. Zhang, L. Liao and A. Qin, *Inorganics*, 2025, **13**, 225.
29 H. Yu, R. Shi, Y. Zhao, T. Bian, Y. Zhao, C. Zhou, G. I. N. Waterhouse, L. Wu, C. Tung and T. Zhang, *Adv. Mater.*, 2017, **29**, 1605148.
30 H. Chen, W. Wang, Z. Yang, X. Suo, Z. Lu, W. Xiao and S. Dai, *J. Mater. Chem. A*, 2021, **9**, 4700–4706.
31 W. Tu, Y. Xu, J. Wang, B. Zhang, T. Zhou, S. Yin, S. Wu, C. Li, Y. Huang, Y. Zhou, Z. Zou, J. Robertson, M. Kraft and R. Xu, *ACS Sustainable Chem. Eng.*, 2017, **5**, 7260–7268.
32 W. Xing, K. Cheng, Y. Zhang, J. Ran and G. Wu, *Nanomaterials*, 2021, **11**, 1480.
33 F. Lin, T. Wang, Z. Ren, X. Cai, Y. Wang, J. Chen, J. Wang, S. Zang, F. Mao and L. Lv, *J. Colloid Interface Sci.*, 2023, **636**, 223–229.
34 X. Liu, W. Kang, W. Zeng, Y. Zhang, L. Qi, F. Ling, L. Fang, Q. Chen and M. Zhou, *Appl. Surf. Sci.*, 2020, **499**, 143994.
35 H. Chai, W. Chen, Z. Feng, Y. Li, M. Zhao, J. Shi, Y. Tang and X. Dai, *Nanomaterials*, 2023, **13**, 1433.
36 A. Martn-Recio, C. Romero-Muñiz, A. J. Martnez-Galera, P. Pou, R. Pérez and J. M. Gómez-Rodrguez, *Nanoscale*, 2015, **7**, 11300–11309.
37 R. Singh, D. Scheinecker, U. Ludacka and J. Kotakoski, *Nanomaterials*, 2022, **12**, 3562.
38 M. M. Mridha, S. Kellici and J. Buckeridge, *J. Phys. Chem. C*, 2025, **129**, 15109–15121.
39 S. K. Jain, G. T. Barkema, N. Mousseau, C.-M. Fang and M. A. van Huis, *J. Phys. Chem. C*, 2015, **119**, 9646–9655.
40 L. M. Azofra, D. R. MacFarlane and C. Sun, *Phys. Chem. Chem. Phys.*, 2016, **18**, 18507–18514.
41 S. Hou, X. Gao, X. Lv, Y. Zhao, X. Yin, Y. Liu, J. Fang, X. Yu, X. Ma and T. Ma, *et al.*, *Nano-Micro Lett.*, 2024, **16**, 70.
42 H. Zhai, P. Tan, L. Lu, H. Liu, Y. Liu and J. Pan, *Catal. Sci. Technol.*, 2021, **11**, 3914–3924.
43 Y. Li, M. Ti, D. Zhao, Y. Zhang, L. Wu and Y. He, *J. Alloys Compd.*, 2021, **870**, 159298.
44 J.-Y. Tang, X. Y. Kong, B.-J. Ng, Y.-H. Chew, A. R. Mohamed and S.-P. Chai, *Catal. Sci. Technol.*, 2019, **9**, 2335–2343.
45 Y. Huang, T. Ding, W. Zuo, Z. Nie, M. Zheng and Y. Zeng, *Environ. Res.*, 2025, **274**, 121302.
46 G. Dong, W. Ho and C. Wang, *J. Mater. Chem. A*, 2015, **3**, 23435–23441.
47 H. Shang, X. Ye, H. Jia, Q. Zhu, D. Zhang, D. Wang and G. Li, *Adv. Mater. Technol.*, 2023, **8**, 2201579.
48 L. Hou, X. Cui, B. Guan, S. Wang, R. Li, Y. Liu, D. Zhu and J. Zheng, *Nature*, 2022, **606**, 507–510.
49 Q. Zhu and J. Zhang, *Environ. Funct. Mater.*, 2022, **1**, 121–125.
50 A. Capobianco, J. Wiktor, A. Landi, F. Ambrosio and A. Peluso, *Nano Lett.*, 2024, **24**, 8335–8342.
51 A. Landi, F. Ambrosio, A. Leo, D. Padula, G. Prampolini and A. Peluso, *J. Mater. Chem. C*, 2025, **13**, 23855–23869.
52 F. Ambrosio, J. Wiktor, A. Landi and A. Peluso, *J. Phys. Chem. Lett.*, 2023, **14**, 3343–3351.
53 D. M. Teter and R. J. Hemley, *Science*, 1996, **271**, 53–55.
54 E. Kroke and M. Schwarz, *Coord. Chem. Rev.*, 2004, **248**, 493–532.
55 P. C. Hohenberg, *Phys. Rev.*, 1967, **158**, 383.
56 N. D. Mermin and H. Wagner, *Phys. Rev. Lett.*, 1966, **17**, 1133.
57 A. S. Ivanov, E. Miller, A. I. Boldyrev, Y. Kameoka, T. Sato and K. Tanaka, *J. Phys. Chem. C*, 2015, **119**, 12008–12015.
58 J. Wang, D. Hao, J. Ye and N. Umezawa, *Chem. Mater.*, 2017, **29**, 2694–2707.
59 T. Möslinger, N. Österbacka and J. Wiktor, *J. Phys. Chem. Lett.*, 2025, **16**, 6861–6865.
60 X. Bi, L.-Z. Wang, D.-H. Zhai, L. Wang, H. Yang and G.-H. Du, *Sci. Rep.*, 2025, **15**, 19864.
61 F. Ambrosio and J. Wiktor, *Appl. Phys. Lett.*, 2025, **126**, 130501.
62 A. Actis, M. Melchionna, G. Filippini, P. Fornasiero, M. Prato, M. Chiesa and E. Salvadori, *Angew. Chem., Int. Ed.*, 2023, **62**, e202313540.
63 X. Bi, L.-Z. Wang, D.-H. Zhai, L. Wang, H. Yang and G.-H. Du, *Sci. Rep.*, 2025, **15**, 19864.
64 C. Freysoldt, J. Neugebauer and C. G. Van de Walle, *Phys. Rev. Lett.*, 2009, **102**, 016402.
65 H.-P. Komsa, T. T. Rantala and A. Pasquarello, *Phys. Rev. B: Condens. Matter Mater. Phys.*, 2012, **86**, 045112.
66 M. Loriso, S. Azmat, A. Listorti, A. Landi, J. Wiktor, F. De Angelis, A. Peluso, S. Colella and F. Ambrosio, *J. Phys. Energy*, 2025, **8**, 015009.
67 F. Ambrosio, G. Miceli and A. Pasquarello, *J. Chem. Phys.*, 2015, **143**, 244508.
68 F. Ambrosio, W. Chen and A. Pasquarello, *Phys. Chem. Chem. Phys.*, 2025, **27**, 23079–23090.

